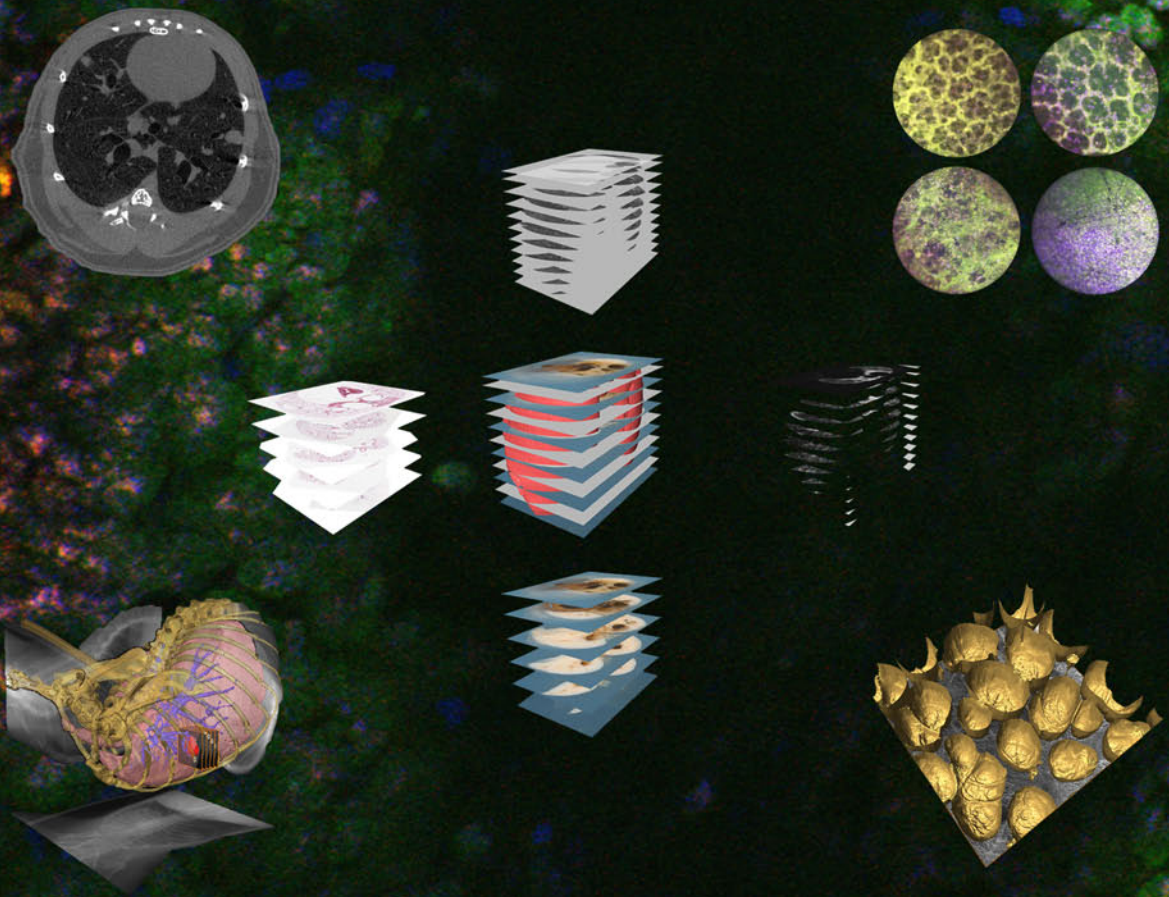


Pre-Clinical Multi-Modal Imaging for Assessment of Pulmonary Structure, Function and Pathology



Eman Namati

**Pre-Clinical Multi-Modal Imaging
for Assessment of Pulmonary
Structure, Function and
Pathology**

by

Eman Namati

Thesis submitted for the degree of

Doctor of Philosophy

in

Biomedical Engineering

Flinders University, Adelaide, Australia

2008

Research Supervisor: **Professor Geoffrey McLennan, M.D., Ph.D.**
University of Iowa, Iowa City, USA

Academic Supervisor: **Professor Murk Bottema, Ph.D.**
Flinders University, Adelaide, Australia

The research described in this thesis was conducted at the University of Iowa under the Translational Lung Imaging Research Program (TLIRP) and the Iowa/South Australia Transnational Alliance (ISATNA).



Contents

Abstract	ix
Declaration.....	xi
Acknowledgments	xii
Publications.....	xiii
List of Figures.....	xviii
List of Tables	xxxi
List of Symbols and Abbreviations.....	xxxii
Chapter 1. Motivation, Significance and Innovation.....	1
1.1 Introduction	1
1.2 Thesis Overview	2
1.2.1 Chapter 2: Background.....	3
1.2.2 Chapter 3: 3D Lung Pathology Imaging.....	3
1.2.3 Chapter 4: Micro Computed Tomography Lung Imaging.....	4
1.2.4 Chapter 5: Laser Scanning Confocal Microscopy Lung Imaging.....	4
1.2.5 Chapter 6: Longitudinal Multi-Modal Assesment of Lung Cancer	5
1.3 Conclusion.....	6
1.4 Statement of Original Contributions.....	7
Chapter 2. Background.....	10
2.1 Lung Structure and Function.....	10
2.1.1 Introduction.....	10
2.1.2 Ventilation	11
2.1.3 Perfusion.....	15
2.1.4 Defense Mechanism	16
2.1.5 Conclusion	16
2.2 Microscopic Pathology Imaging.....	17
2.2.1 Introduction.....	17
2.2.2 Pulmonary Histopathology	17
2.2.3 Conclusion	19
2.3 Micro-CT Imaging.....	20

2.3.1	Introduction.....	20
2.3.2	X-ray Imaging.....	21
2.3.3	Image Reconstruction.....	27
2.3.4	Micro Computed Tomography.....	35
2.3.5	Conclusions.....	38
2.4	Laser Scanning Confocal Microscopy.....	40
2.4.1	Introduction.....	40
2.4.2	Confocal Microscopy.....	41
2.4.3	Catheter-Based Confocal Microscopy.....	50
2.4.4	Conclusions.....	54
2.5	Mouse Models of Lung Cancer.....	56
2.5.1	Introduction.....	56
2.5.2	Spontaneous and Carcinogenic Models.....	57
2.5.3	Genetically Manipulated Models.....	61
2.5.4	Conclusions.....	63
Chapter 3. 3D Lung Pathology Imaging.....		66
3.1	Introduction.....	66
3.2	Methods.....	68
3.2.1	Microtome Development.....	68
3.2.2	Microtome Motorization.....	69
3.2.3	Vibrating Blade Microtome Development.....	70
3.2.4	Photo Lock.....	71
3.2.5	Imaging System.....	72
3.2.6	Automation Software.....	73
3.2.7	Lung Tissue Preparation.....	75
3.2.8	Mouse Lung Agarose Embedding.....	76
3.2.9	Solid Tissue Preparation.....	76
3.2.10	Standard Histology and Immunohistochemical Staining.....	76
3.2.11	Image Acquisition.....	76
3.3	Results.....	78
3.3.1	Fixed Sheep Lung Specimens.....	78

3.3.2	Fixed Mouse Lung Specimens.....	79
3.4	Discussion	83
3.5	Conclusion.....	85
Chapter 4. Micro-CT Lung Imaging		87
4.1	Introduction	87
4.2	Micro-CT Artifact Reduction and Image Processing.....	89
4.2.1	Introduction.....	89
4.2.2	Methods and Materials	90
4.2.3	Results	100
4.2.4	Discussion.....	105
4.2.5	Conclusion	107
4.3	In Vivo Lung Imaging.....	108
4.3.1	Introduction.....	108
4.3.2	Methods and Materials	109
4.3.3	Results	117
4.3.4	Discussion.....	126
4.3.5	Conclusions.....	127
Chapter 5. LSCM Lung Imaging		130
5.1	Introduction	130
5.2	Ex Vivo Lung Imaging.....	132
5.2.1	Introduction.....	132
5.2.2	Methods and Materials	134
5.2.3	Results	138
5.2.4	Discussion.....	143
5.2.5	Conclusion	149
5.3	In Vivo Lung Imaging.....	150
5.3.1	Introduction.....	150
5.3.2	Methods and Materials	151
5.3.3	Results	157
5.3.4	Discussion.....	160
5.3.5	Conclusions.....	161

Chapter 6. Longitudinal Multi-Modal Assessment of Lung Cancer	164
6.1 Introduction	164
6.2 Material and Methods	166
6.2.1 Micro-CT Imaging Heating Chamber	166
6.2.2 Flexible Miniature Mouse Bronchoscope.....	167
6.2.3 Portable Micro-Controller Ventilator	169
6.2.4 Animal Preparation.....	170
6.2.5 Study Timeline.....	174
6.2.6 Multi-Modal Image Acquisition	175
6.2.7 Image Processing.....	185
6.2.8 Image Analysis.....	186
6.2.9 Multi-Modal Registration	190
6.3 Results	193
6.3.1 Micro-CT Imaging	193
6.3.2 PET and MRI Imaging	207
6.3.3 CBCM and LSCM Imaging.....	209
6.3.4 LIMA Imaging	215
6.3.5 Histology.....	220
6.4 Discussion	223
6.4.1 Image Acquisition	223
6.4.2 Micro-CT Tumor Analysis	225
6.4.3 Micro-PET & MRI.....	229
6.4.4 LSCM Imaging.....	231
6.4.5 LIMA Imaging	235
6.4.6 Histology.....	237
6.5 Conclusions	239
Chapter 7. Summary and Future Direction.....	242
7.1 Summary and Future Direction	242
Bibliography	248
Appendix A	264
Appendix B	265

Appendix C 310
Appendix D 313

Abstract

In this thesis, we describe several imaging techniques specifically designed and developed for the assessment of pulmonary structure, function and pathology. We then describe the application of this technology within appropriate biological systems, including the identification, tracking and assessment of lung tumors in a mouse model of lung cancer.

The design and development of a Large Image Microscope Array (LIMA), an integrated whole organ serial sectioning and imaging system, is described with emphasis on whole lung tissue. This system provides a means for acquiring 3D pathology of fixed whole lung specimens with no infiltrative embedment medium using a purpose-built vibratome and imaging system. This system enables spatial correspondence between histology and non-invasive imaging modalities such as Computed Tomography (CT), Magnetic Resonance Imaging (MRI) and Positron Emission Tomography (PET), providing precise correlation of the underlying “ground truth” pathology back to the *in vivo* imaging data. The LIMA system is evaluated using fixed lung specimens from sheep and mice, resulting in large, high-quality pathology datasets that are accurately registered to their respective CT and H&E histology.

The implementation of an *in vivo* micro-CT imaging system in the context of pulmonary imaging is described. Several techniques are initially developed to reduce artifacts commonly associated with commercial micro-CT systems, including geometric gantry calibration, ring artifact reduction and beam hardening correction. A computer controlled Intermittent Iso-pressure Breath Hold (IIBH) ventilation system is then developed for reduction of respiratory motion artifacts in live, breathing mice. A study validating the repeatability of extracting valuable pulmonary metrics using this technique against standard respiratory gating techniques is then presented.

The development of an *ex vivo* laser scanning confocal microscopy (LSCM) and an *in vivo* catheter based confocal microscopy (CBCM) pulmonary imaging technique is described. Direct high-resolution imaging of sub-pleural alveoli is presented and

an alveolar mechanic study is undertaken. Through direct quantitative assessment of alveoli during inflation and deflation, recruitment and de-recruitment of alveoli is quantitatively measured. Based on the empirical data obtained in this study, a new theory on alveolar mechanics is proposed.

Finally, a longitudinal mouse lung cancer study utilizing the imaging techniques described and developed throughout this thesis is presented. Lung tumors are identified, tracked and analyzed over a 6-month period using a combination of micro-CT, micro-PET, micro-MRI, LSCM, CBCM, LIMA and H&E histology imaging. The growth rate of individual tumors is measured using the micro-CT data and traced back to the histology using the LIMA system. A significant difference in tumor growth rates within mice is observed, including slow growing, regressive, disappearing and aggressive tumors, while no difference between the phenotype of tumors was found from the H&E histology. Micro-PET and micro-MRI imaging was conducted at the 6-month time point and revealed the limitation of these systems for detection of small lesions (<2mm) in this mouse model of lung cancer. The CBCM imaging provided the first high-resolution live pathology of this mouse model of lung cancer and revealed distinct differences between normal, suspicious and tumor regions. In addition, a difference was found between control A/J mice parenchyma and Urethane A/J mice ‘normal’ parenchyma, suggesting a “field effect” as a result of the Urethane administration and/or tumor burden. In conclusion, a comprehensive murine lung cancer imaging study was undertaken, and new information regarding the progression of tumors over time has been revealed.

Declaration

I certify that this thesis does not incorporate without acknowledgment any material previously submitted for a degree or diploma in any university; and that to the best of my knowledge and belief it does not contain any material previously published or written by another person except where due reference is made in the text.

A handwritten signature in black ink, appearing to read 'EMAN NAMATI', written in a cursive style with a large initial 'E' and 'N'.

Eman Namati

Acknowledgments

This large collection of work could not have been accomplished without the help of many individuals who I would like to sincerely thank.

First and foremost I would like to thank my primary supervisor Professor Geoffrey McLennan for his continual support, encouragement and enthusiasm. During this time he provided direction and advice both academically as a professional, and as a friend, for whom I will always be grateful.

I would also like to thank Professor Murk Bottema for all of his academic guidance and great discussions. I could not have had a better transnational academic supervisor, thank you.

I would like to acknowledge the following individuals for their help, advice and collaboration throughout my doctoral program, Prof. Eric A. Hoffman, Prof. Alan Ross, Prof. Michael J. Welsh, Prof. Joeseeph Zabner, Prof. Milan Sonka, Prof. Daniel Thedens, Dr Deokiee Chon, Dr Melissa Suter, Dr Osama Saba, Dr David Stoltz, Dr Shaun S Gleason, Jacqueline Thiesse, Jessica de Ryk, Zaid Towfic, Amanda Smith, Andrew Stessman, Jered Sierens, Keith Brautigham, Michael Wardenburg, Peter Taft, Thomas Moninger, and Susan Walsh.

I would like to deeply thank my parents Mohammad and Akram Namati, for bringing me to Australia and encouraging me to think, discover and learn, even when it got me in trouble!

I would also like to thank all my family and friends both in Australia and in the United States, who have helped me through this endeavor with positive enthusiasm.

I would finally like to thank my wife, Jacqueline Rose Thiesse. Initially for being a great friend and now a wonderful partner. Thank you for getting me through the hard times, and sharing all the great times. I love you!

Publications

International Journal Articles (in chronological order).

[1] **Namati, E.**, Chon, D., Thiesse, J., Hoffman, E. A., de Ryk, J., Ross, A., and McLennan, G., "In vivo micro-CT lung imaging via a computer-controlled intermittent iso-pressure breath hold (IIBH) technique," *Phys Med Biol*, vol. 51, pp. 6061-75, 2006

[2] de Ryk, J., Thiesse, J., **Namati, E.**, and McLennan, G., "Stress distribution in a three dimensional, geometric alveolar sac under normal and emphysematous conditions," *Int J Chron Obstruct Pulmon Dis*, vol. 2, pp. 81-91, 2007

[3] **Namati, E.**, De Ryk, J., Thiesse, J., Towfic, Z., Hoffman, E., and McLennan, G., "Large image microscope array for the compilation of multimodality whole organ image databases," *Anat Rec (Hoboken)*, vol. 290, pp. 1377-87, 2007

[4] Baker, K. M., **Namati, E.**, Hoffman, E., Van Beek, E. J. R., Ross, A., and McLennan, G., "Virtual bronchoscopy: new applications for MDCT in pulmonology," *Advances in MDCT*, vol. 3, pp. 10-18, 2007

[5] McLennan, G., **Namati, E.**, Ganatra, J., Suter, M., O'Brien, E. E., Lecamwasam, K., Van Beek, E. J. R., and Hoffman, E., "Virtual Bronchoscopy," *MRI*, vol. 11, pp. 10-20, 2007

[6] **Namati, E.**, Thiesse, J., de Ryk, J., and McLennan, G., "Alveolar Dynamics during Respiration: Are the Pores of Kohn a Pathway to Recruitment?," *Am J Respir Cell Mol Biol*, vol. 38, pp. 572-8, 2008

[7] Rogers, C. S., Abraham, W. M., Brogden, K. A., Engelhardt, J. F., Fisher, J. T., McCray Jr, P. B., McLennan, G., Meyerholz, D. K., **Namati, E.**, Ostedgaard, L. S., Prather, R. S., Sabater, J. R., Stoltz, D. A., Zabner, J., and Welsh, M. J., "The Porcine Lung as a Potential Model for Cystic Fibrosis," *Am J Physiol Lung Cell Mol Physiol*, 2008

International Conference Proceedings (in chronological order).

[1] **Namati, E.**, de Ryk, J., McLennan, G., Hoffman, E., and Piker, C., "A Novel Whole-organ Serial Sectioning and Image Acquisition System.," presented at 2003 World Congress on Biomedical Engineering Proceedings, Sydney, Australia, 2003.

[2] Thiesse, J. R., **Namati, E.**, de Ryk, J., Hoffman, E. A., and McLennan, G., "Bright field segmentation tomography (BFST) for use as surface identification in stereomicroscopy," presented at Three-Dimensional and Multidimensional Microscopy: Image Acquisition and Processing XI, San Jose, CA, USA, 2004.

[3] de Ryk, J., **Namati, E.**, Reinhardt, J. M., Piker, C., Xu, Y., Liu, L., Hoffman, E. A., and McLennan, G., "A whole organ serial sectioning and imaging system for correlation of pathology to computer tomography," presented at Three-Dimensional and Multidimensional Microscopy: Image Acquisition and Processing XI, San Jose, CA, USA, 2004.

[4] **Namati, E.** and Li, J., "A Novel Shape Descriptor Based on Empty Morphological Skeleton Subsets," presented at 2004 International Symposium on Intelligent Multimedia, Video and Speech Processing, Hong Kong, 2004.

[5] Thiesse, J., Reinhardt, J. M., de Ryk, J., **Namati, E.**, Leinen, J., Recheis, W. A., Hoffman, E. A., and McLennan, G., "Three-dimensional visual truth of the normal airway tree for use as a quantitative comparison to micro-CT reconstructions," presented at Medical Imaging 2005: Physiology, Function, and Structure from Medical Images, San Diego, CA, USA, 2005.

[6] Thiesse, J. R., de Ryk, J., Bond, S., Vislisel, J., Hoffman, E., **Namati, E.**, Reinhardt, J., and McLennan, G., "Assessment of mouse lung fixation pressures using computed tomography," presented at American Thoracic Society, San Diego, CA, 2005.

[7] de Ryk, J., Thiesse, J. R., **Namati, E.**, Reinhardt, J., Hoffman, E., and McLennan, G., "A novel microscopy system for Assessing the Accuracy of CT in soft tissue diagnostic imaging," presented at American Thoracic Society, San Diego, CA, 2005.

[8] **Namati, E.**, Chon, D., Thiesse, J., McLennan, G., Sieren, J., Ross, A., and Hoffman, E. A., "In vivo micro-CT imaging of the murine lung via a computer controlled intermittent iso-pressure breath hold (IIBH) technique," presented at Medical Imaging 2006: Physiology, Function, and Structure from Medical Images, San Diego, CA, USA, 2006.

[9] **Namati, E.**, Chon, D., Thiesse, J., Ross, A., McLennan, G., and Hoffman, E. A., "Comparison of Four Micro-CT Gating Techniques for Physiologic and Anatomical Analysis of Mouse Lungs In-Vivo," presented at American Thoracic Society, San Diego, CA, 2006.

[10] Chon, D., **Namati, E.**, Fuld, M. K., Sieren, J., McLennan, G., and Hoffman, E. A., "In Vivo Assessment of Regional Lung Function in Mice Via Micro CT," presented at American Thoracic Society, San Diego, CA, 2006.

[11] Thiesse, J., **Namati, E.**, de Ryk, J., Hoffman, E., Reinhardt, J., and McLennan, G., "Three Dimensional Anatomical Description of the Normal Airway Tree in Three Strains of Mice," presented at Society for Molecular Imaging, Hawaii, Big Island, 2006.

[12] **Namati, E.**, Chon, D., Thiesse, J., Hoffman, E. A., Ross, A., and McLennan, G., "In vivo micro-CT imaging of mice lungs using a novel breath hold technique," presented at Society for Molecular Imaging, Hawaii, Big Island, 2006.

[13] **Namati, E.**, Thiesse, J., de Ryk, J., and McLennan, G., "Dynamic in vivo Alveolar Morphology Using a Novel Laser Scanning Confocal Microscope," presented at 9th Biennial Conference of the Australian Pattern Recognition Society on Digital Image Computing Techniques and Applications (DICTA 2007), Adelaide, Australia, 2007.

- [14] de Ryk, J., Weydert, J., Thiesse, J., **Namati, E.**, Reinhardt, J., Lynch, W., and McLennan, G., "Lung Adenocarcinoma: 3D Tissue Content and Distribution," presented at American Thoracic Society, San Francisco, CA, 2007.
- [15] **Namati, E.**, Thiesse, J., de Ryk, J., and McLennan, G., "Imaging of Fresh Intact Mice Lungs during Respiration," presented at American Thoracic Society, San Francisco, CA, 2007.
- [16] de Ryk, J., Raghavan, M., Reinhardt, J., Thiesse, J., **Namati, E.**, and McLennan, G., "A Finite Element Model of the Human Alveolar Sac to Investigate Normal and Emphysematous States," presented at American Thoracic Society, San Francisco, CA, 2007.
- [17] Thiesse, J., **Namati, E.**, de Ryk, J., Reinhardt, J., Hoffman, E., and McLennan, G., "3D Anatomy of the Normal Airway Tree in Three Strains of Mice Using Micro-CT and Pathology Techniques," presented at American Thoracic Society, San Francisco, CA, 2007.
- [18] **Namati, E.**, Thiesse, J., de Ryk, J., and McLennan, G., "In vivo imaging of alveoli," presented at American Thoracic Society, San Francisco, CA, 2007.
- [19] O'Brien, E. E., Reinhardt, J., Towfic, Z., **Namati, E.**, Ferguson, J. S., and McLennan, G., "Quantitative Color and Texture Analysis of Human Airways," presented at American Thoracic Society, San Francisco, CA, 2007.
- [20] de Ryk, J., Weydert, J., Christensen, G., Thiesse, J., **Namati, E.**, Reinhardt, J., Hoffman, E., and McLennan, G., "Three-dimensional histopathology of lung cancer with multimodality image registration," presented at Medical Imaging 2007: Image Processing, San Diego, CA, USA, 2007.
- [21] **Namati, E.**, Thiesse, J., de Ryk, J., and McLennan, G., "In vivo and ex vivo imaging of alveolar structure and function using a custom fiber optic laser scanning

confocal microscope," presented at Medical Imaging 2008: Physiology, Function, and Structure from Medical Images, San Diego, CA, USA, 2008.

[22] de Ryk, J., **Namati, E.**, Thiesse, J., Reinhardt, J., Hoffman, E., and McLennan, G., "Establishment of a Process Model for the Collection of Multi-Modality Data Relating to Human Lung Cancer Nodules," presented at American Thoracic Society, Toronto, Canada, 2008.

[23] **Namati, E.**, Thiesse, J., de Ryk, J., and McLennan, G., "Longitudinal Multi-Modality Three-Dimensional Imaging of Lung Cancer in Mice," presented at American Thoracic Society, Toronto, Canada, 2008.

[24] Thiesse, J., **Namati, E.**, de Ryk, J., Reinhardt, J., Hoffman, E., Shi, L., and McLennan, G., "Phenotype Characterization of the Normal Lung in Three Strains of Mice Using Micro-CT and 3D Microscopy Techniques," presented at American Thoracic Society, Toronto, Canada, 2008.

[25] de Ryk, J., Thiesse, J., **Namati, E.**, Weydert, J., Reinhardt, J., Hoffman, E., and McLennan, G., "Automated Classification of Lung Cancer Histopathology with 3D Correlation to Density Representation in CT," presented at American Thoracic Society, Toronto, Canada, 2008.

[26] **Namati, E.**, Thiesse, J., de Ryk, J., and McLennan, G., "In Vivo Catheter-Based Histopathology of Lung Cancer in Mice," presented at American Thoracic Society, Toronto, Canada, 2008.

List of Figures

Figure 2.1: The human respiratory system, [8].....	11
Figure 2.2: Cascading airway structure, Adapted from [9, 11].....	13
Figure 2.3: Cross sectional area vs. airway generation number, [9].....	13
Figure 2.4: Alveolar structure, with permission from [16].....	14
Figure 2.5: Schematic of ventilation and perfusion through the human lung, [9]....	15
Figure 2.6: Sheep lung fixed using the Heitzman technique, a) dorsal, b) ventral and c) Left lateral view.....	19
Figure 2.7: Schematic example of an X-ray source.....	24
Figure 2.8: CCD readout flow diagram.....	25
Figure 2.9: Geometry co-ordinate system, recreated from [38].	28
Figure 2.10: $F(u,v)$ the Fourier transform of the object $f(x,y)$ along radial lines attained through projections of the object at discrete angles, recreated from [38].....	31
Figure 2.11: Comparison of reconstruction with 4, 8 & 16 projections.....	33
Figure 2.12: Shepp-Logan, Ram-Lak and Hamming convolution filters, where zero frequency is at the center of the x-axis.	33
Figure 2.13: Typical micro computed tomography cone-beam geometry.....	36
Figure 2.14: Ring artifact example from a micro-CT water phantom scan.....	37
Figure 2.15: Marvin Minsky's 1961 Confocal Microscope patent.....	41
Figure 2.16: Simplified confocal microscope schematic diagram [45].	42
Figure 2.17: Two dimensional galvanometer scan head, modified from [46].	43
Figure 2.18: Quantum Efficiency comparison across a variety of light detecting devices, modified from [47].....	45
Figure 2.19: Photomultiplier schematic diagram, modified from [48].	45
Figure 2.20: Airy disk pattern, left: top view, right: side profile, modified from [46].	48

- Figure 2.21: Light scanning techniques: (a-c) Proximal Scanning, (a) Cascaded galvanometer mirror couple used to scan the excitation and emission beam across the proximal end of a fiber bundle. (b) Proximal line scanning using a cylindrical lens to focus the illumination into a line, scanning the face of a fiber bundle one line at a time. (c) Proximal scanning using a spatial light modulator, which illuminates each pixel sequentially with a stationary excitation beam. (d-f) Distal Scanning, (d) Distal 2D mirror scanning using a piezo-electric mirror or a MEMS mirror setup. (e) Distal fiber tip scanning where the tip of the excitation fiber is vibrated at resonance to achieve a scanning pattern. (f) Distal fiber-objective scanning where both the fiber and the objective lens couple are vibrated at resonance. Modified from [70]...... 51
- Figure 2.22: Coherent imaging fiber bundle illustration, modified from [73]...... 52
- Figure 2.23: (left) Magnified view (bar equals 500 μ m) of a MEMS mirror [70], (right) dual-axis confocal micro-endoscope head incorporating MEMS mirror [67]...... 52
- Figure 2.24: Virtual Bronchoscopy with path finding to a peripheral location..... 54
- Figure 2.25: Metabolic activation of ethyl carbamate to DNA adducts in the mouse lung, modified from [86]...... 58
- Figure 2.26: Timeline of lung tumor carcinogenesis in the Urethane-induced lung cancer model, recreated from [109]...... 60
- Figure 3.1: The large image microscope array (LIMA) system shown with; a CCD digital camera mounted to a stereomicroscope, which are both positioned over the specimen stage via a gantry to image the tissue en bloc..... 69
- Figure 3.2: (a) represents a schematic of the large-scale dual-frequency vibrating knife system from a top and side view. (b) a pictorial representation of the low frequency motion through rotation of the motor assembly and high frequency motion as depicted by the waves protruding from the linear air vibrator..... 71
- Figure 3.3: (a) shows the microtome and locking mechanism (on the left) that ensures correct positioning of the stage for image acquisition. (b) shows a close up of the “photo locking” mechanism prior to an imaging sequence..... 72

- Figure 3.4: The graphical user interface used to control the functions of the LIMA system. (a) the tissue setup phase, where the user interactively selects the area of the microtome stage that includes the tissue specimen. (b) the image preparation step, where the user interactively determines the centre of the tissue specimen, along with the magnification, field of view and boundaries for image acquisition. (c) left panel shows the current high magnification image which is being captured and the right panel shows the completed montage of the sub-images. 74
- Figure 3.5: Sheep (a-b) and mouse (c-d) lung fixed using the Heitzman technique. Scale bar for (a-b) is 100mm and (c-d) is 5mm. 75
- Figure 3.6: (a) represents a CT slice from the upper lobe of a fixed sheep lung and figure 5 (b) represents the corresponding stitched LIMA image. 78
- Figure 3.7: An example application of the LIMA system for the registration of a multi-modal fixed sheep lung dataset. (a) represents the color LIMA image, (b) represents the micro-CT radiological image and finally (c) represents the H&E histopathology image, from the same location. The images have been registered using a thin-plate spline algorithm and the final multi-modal dataset provides registered radio-density, color and cellular information. In (d) and (e), a small area to the left of images (a-b) has been magnified to reveal the strong correlation between the registered H&E histology and micro-CT image with respect to the LIMA dataset. 79
- Figure 3.8: Mouse lung mounted inside the Micro-CT and LIMA static orientation device. 80
- Figure 3.9: Image acquisition and registration pipeline using the *ex vivo* micro-CT and LIMA datasets as the reference. 81
- Figure 3.10: An example of a registered mouse lung dataset from the *in vivo* state down to the histology level can be seen. (a) represents a 28-micron slice from the original *in vivo* micro-computed tomography scan. (b) represents a 28-micron slice from the fixed *ex vivo* micro-computed tomography scan. (c) represents a final LIMA image, stitched from 49 sub-images at 40x magnification. Finally, (d) represents the corresponding H&E histopathology image for the same slice. In this example we can see the advantage of the

LIMA system in providing spatial correlation between a non-destructive three-dimensional modality such as the micro-CT with respect to the destructive histopathology imaging.....	82
Figure 3.11: 3D representation of the entire mouse lung boundary obtained from the LIMA system is shown; clearly the non iso-tropic nature of this imaging system is evident by the jarred edges between slices.....	82
Figure 4.1: Siemens MicroCAT-II micro-Computed Tomography scanner.....	90
Figure 4.2: Brass ball bearing phantom encased in polyurethane foam.....	91
Figure 4.3: Schematic geometric illustration for calculating the source-to-object and source-to-detector distance using the ball bearing phantom X-ray projections at two known distances.....	92
Figure 4.4: Ball phantom projection, a) position 1 – closer to detector, b) position 2 – closer to source.....	93
Figure 4.5: Change in projected ball phantom diameter in mm (y-axis) over 360 degrees (x-axis).	94
Figure 4.6: Calculated change in object position with respect to source and detector in mm (y-axis) over 360 degrees (x-axis).....	94
Figure 4.7: a) original sinogram with average column intensity profile (red), smoothed profile (black) and difference between the normal and smoothed profile (blue), b) original sinogram with filter applied c) calibrated sinogram with average column intensity profile (red), smoothed profile (black) and difference between the normal and smoothed profile (blue), d) calibrated sinogram with filter applied.....	96
Figure 4.8: Magnified sinogram, a) original sinogram, b) original sinogram with average column intensity profile (red), smoothed profile (black) and difference between the normal and smoothed profile (blue), b) original sinogram with filter applied.	96
Figure 4.9: Water phantom scan with no hardware filter.....	97
Figure 4.10: Water phantom scan with 3mm Aluminum filter.....	98

Figure 4.11: (a) Beam hardening correction phantom and (b) representative projection X-ray image.....	99
Figure 4.12: (a) log calibrated projection X-ray of the water phantom with 0.5mm Al filter, (b) attenuation profile plot across the varying thickness material as depicted in the red line in (a).....	99
Figure 4.13: Ex vivo lung axial slice, a) normal reconstruction, b) reconstruction with dynamic source to detector distance.....	101
Figure 4.14: Ex vivo fixed lung axial slice, (a) normal reconstruction, (b) reconstruction with dynamic center offset distance.....	101
Figure 4.15: a) Original axial lung image with moderately severe ring artifacts, b) image a) post ring artifact reduction, c) Original axial lung image with moderate ring artifacts, d) image c) post ring artifact reduction.....	102
Figure 4.16: Beam hardening water phantom, (a) 1 cm phantom axial slice, (b) 2 cm phantom axial slice and (c) 3 cm phantom axial slice, red line shown for location of profile plots in Figure 4.17.....	103
Figure 4.17: Profile plot across red line shown in Figure 4.16 (a-c) for water phantom at 1, 2 & 3cm thickness.....	104
Figure 4.18: Corrected beam hardening water phantom, (a) 1 cm phantom axial slice, (b) 2 cm phantom axial slice and (c) 3 cm phantom axial slice, red line shown for location of profile plots in Figure 4.19.....	104
Figure 4.19: Profile plot across red line shown in Figure 4.18 (a-c) for corrected water phantom at 1, 2 & 3cm thickness.....	105
Figure 4.20: Scireq Flexivent small animal computer-controlled ventilator.....	110
Figure 4.21. Respiratory Gating System Block Diagram. --- Dotted lines represent pneumatic pipeline. S - represents electronic controlled solenoids.....	111
Figure 4.22. Late Inspiratory (solid) and Late Expiratory (dashed) gating waveform schematic.....	112
Figure 4.23: IIBH breathing sequence; hyperventilated breathing, two deep breaths (sighs) and no ventilation, triggering of a forced airway pressure (breath-hold),	

at which time the Micro-CT is triggered and multiple angles of view are acquired.....	113
Figure 4.24: Mouse tracheotomy – surgical series from left to right.....	114
Figure 4.25. Axial slice gating comparison, a) No Gating, b) LI Gating, c) LE Gating, d) IIBH Gating. (window level -1000 to 2000 HU).....	118
Figure 4.26: Coronal density profile, a) No Gating, b) LI Gating, c) LE Gating, d) IIBH Gating.....	119
Figure 4.27: Density Profile of Lung-Abdomen Interface.	120
Figure 4.28: Right Main Bronchus Density Profile, a) No Gating, b) LI Gating, c) LE Gating, d) IIBH Gating.	121
Figure 4.29: Right main bronchus density profile plot.	121
Figure 4.30: 3D reconstruction of the mouse lung and spine. Note the clear delineation of the ribs as well as lobar fissures and diaphragmatic surface indicating very accurate gating during scanning of a live breathing mouse...	122
Figure 4.31: (a) No gating, (b) LI gating, (c) LE gating, (d) IIBH gating volume repeatability curve (centerline represents mean, dotted lines represent two standard deviations).....	123
Figure 4.32: (a) No Gating, (b) LI Gating, (c) LE Gating, (d) IIBH Gating Air Content repeatability curve (centerline represents mean, dotted lines represent two standard deviations).....	124
Figure 4.33.: a) axial & b) coronal 2D air content of mouse lung with air content color map. As seen in both, the change in air content is very slight, shifting from dependant to non-dependant in the axial and apex to the base in the coronal.	125
Figure 4.34.: a) 3D reconstruction of mouse lung air content with air content color map. b) same as (a) including spine and ribs, red arrows indicate beam hardening effects from the spine and ribs.....	126
Figure 5.1: <i>Ex vivo</i> mouse lung imaging chamber, which is air and water tight to allow measurement of lung volume change.....	135

- Figure 5.2: *Ex vivo* mouse lung imaging schematic, consists of a custom iso-pressure system for inflating the lung to the desired pressure, a commercial Bio-Rad laser scanning confocal microscope and a custom in vitro air and water tight lung imaging chamber. 136
- Figure 5.3: Example of automated intercept labeling. Beginning of a wall is represented by a blue cross and end of a wall by a red cross. Logging of intercepts allows accurate calculation of airspace and wall chord lengths..... 137
- Figure 5.4: Confocal images of the same mouse lung throughout an inflation/deflation cycle. (a)-(h) represent 5 micron thick LSCM sections from the same mouse lung inflated through pressures 0-35 cmH₂O in 5 cmH₂O increments, respectively, and (j)-(o) for deflation. All images were acquired using a 10x objective and field of view of 1.2mmx1.2mm. 140
- Figure 5.5: (a) Change in lung volume vs. pressure, (b) Alveolar airspace number in field of view (1.44mm²) vs. inflation pressure, (c) Mean Chord Length of alveolar airspace vs. inflation pressure, (d) Mean Chord Length of alveolar walls. Error bars represent the standard deviation (+SD) for five mice..... 141
- Figure 5.6: (a) Inflation 0-35 cmH₂O, with wall intercepts. (b) Inflation 0-35 cmH₂O, clustered by color-coded area (μ^2). (c) Inflation 0-35 cmH₂O, histogram of airspace chord lengths (μ). γ_1 =Skew, γ_2 =Kurtosis, red line = median value. 142
- Figure 5.7: (a) Deflation 35-0 cmH₂O, with wall intercepts. (b) Deflation 35-0 cmH₂O, clustered by color-coded area (μ^2). (c) Deflation 35-0 cmH₂O, histogram of wall chord lengths (μ). γ_1 =Skew, γ_2 =Kurtosis, red line = median value..... 143
- Figure 5.8: 3D comparison of sub-pleural alveoli at 10 cmH₂O (top row) and 35 cmH₂O (bottom row) airway pressure. Here, it can be seen that there is minimal compression artifacts at the cover slip interface, where (a) & (d) are looking into the lung through the pleura, (b) & (e) are side views and finally (c) & (f) are looking out of the lung through the parenchyma..... 144
- Figure 5.9: Cartoon depiction of the mother/daughter alveolar hypothesis during the first breath post deflation. During inflation, the mother alveoli incrementally expand with proportional expansion in the alveolar walls and pores of Kohn.

As the surfactant layer over the pores of Kohn becomes thinner and the pressure gradient between the mother and daughter alveoli increases, air passes through to the daughter alveoli. The recruitment of the daughter alveoli leads to a subsequent reduction in the average size of the mother alveoli as more lung volume is distributed. During deflation, the pressure reduces in both the mother and daughter alveoli until the pores of Kohn reduce in diameter and the surfactant layer reforms its seal, trapping the remaining air inside the daughter alveoli and leading to recruitment of the daughter alveoli. Note: pressure values have been extrapolated from the empirical data obtained in the present mouse lung study..... 146

- Figure 5.10: Schematic of the Catheter Based Confocal Microscope system utilizing a commercial Bio-Rad microscope and a custom fiber injection attachment. 152
- Figure 5.11: Distal end of the fiber optic catheter tip imaged against a United States penny, depicting its small size. (<0.9mm diameter)..... 153
- Figure 5.12: (a) CBCM raw fiber image and (b) zoomed region shown in the red box. Note the fiber pattern is clearly apparent..... 153
- Figure 5.13: Image processing flow diagram for filtering CBCM images of alveolar structure..... 154
- Figure 5.14: (a) raw fiber subtracted CBCM image of alveolar structure and (b) two-dimensional FFT of (a)...... 154
- Figure 5.15: (a) original CBCM image of the alveolar structure and (b) the final filtered image. 155
- Figure 5.16: In vivo laser scanning confocal microscopy of alveolar walls with automated wall intercept analysis overlaid..... 156
- Figure 5.17: Outline of image processing steps for calculating alveolar airspace number and size..... 157
- Figure 5.18: In vivo catheter based laser scanning confocal microscopy of alveolar walls – Fluorescein dye..... 158
- Figure 5.19: In vivo catheter based laser scanning confocal microscopy of nuclei – Acridine Orange dye..... 158

Figure 5.20: (a) airspace and wall chord analysis on CBCM alveolar image shown in Figure 5.18. The calculated MCLa is 39 μ m and the MCLw is 12 μ m. (b) area based cluster analysis of CBCM alveolar airspace, where 121 spaces have been identified from small (red) to large (dark-blue).	159
Figure 5.21: Two examples of alveoli ‘popping’ open in C57BL/6 mice lungs expressing GFP. Each frame was captured over 50ms. Acquired using a catheter-based confocal microscopy technique.	160
Figure 6.1: Custom tunnel heating chamber.	167
Figure 6.2: (a) mouse endoscope with optical viewfinder, (b) magnified image of bronchoscope tip against a United States penny.	168
Figure 6.3: Mouse-bronchoscopy - image acquired at the vocal chords, (a) original image, (b) image with dashed outline of vocal chords. Bright red light in the trachea is a result of the snake light placed over the chest wall, and aides in guidance.	168
Figure 6.4: Small animal ventilator with custom respiratory gating micro-controller.	169
Figure 6.5: Custom electronic pressure controller.	170
Figure 6.6: Mouse connected to ECG and Pulse Ox sensors prior to Tracheotomy.	174
Figure 6.7: <i>in vivo</i> CBCM mouse lung imaging setup.	174
Figure 6.8: Gantt chart representing the timeline for the four groups of Urethane mice and single normal group in this study.	175
Figure 6.9: Custom lung embedding equipment including the orientation bracket, foam encasing mold and two-part polyurethane foam.	179
Figure 6.10: Mouse lung suspended with fishing line and tied in place with one suture around the trachea. A second loose suture loop is place around the lung and fishing line in order to maintain lobe positions during embedding.	180
Figure 6.11: Foam encased mouse lung mounted to the base of the orientation bracket.	181

Figure 6.12: Schematic illustration of the <i>ex vivo</i> image acquisition process utilizing the orientation bracket, during (a) micro-CT imaging, (b) LIMA imaging and (c) LIMA sectioning and H&E Histology processing.....	182
Figure 6.13: Siemens OncoCare prototype application used to facilitate in semi-automated segmentation of mouse lung tumors.....	187
Figure 6.14: Nodule segmentation example. Top left panel represents the OncoCare segmentation software. Panels from left to right represent serial transverse serial images of the nodule with illustration of segmentation border in red..	188
Figure 6.15: Multi-modal registration flow diagram.	192
Figure 6.16: (a-d) Coronal micro-CT image from a Urethane mouse lung at 2, 3, 4 and 6-month time points. Red arrows indicate the same tumor progressing over time.....	193
Figure 6.17: Three-dimensional reconstruction of a Urethane mouse depicting the skeletal system (yellow), lung (pink), vasculature (blue) and tumor volume (red).	194
Figure 6.18: (a) magnified view of the tumor volume and surrounding vasculature, (b) tumor volume with representative projection X-rays.....	195
Figure 6.19: Group 3, Mouse 3, RECIST tumor size (mm) versus time for each nodule.	196
Figure 6.20: Group 3, Mouse 3, WHO tumor size (mm) versus time for each nodule.	197
Figure 6.21: Group 3, Mouse 3, tumor volume (μ l) versus time for each nodule..	198
Figure 6.22: Mean number of tumors per mouse, left lung, right apical lobe, right azygous lobe, right diaphragmatic lobe and right cardiac lobe versus number of months after Urethane administration. Error bars represent the SEM.....	199
Figure 6.23: Tumor incidence and lobe volume versus lobe location.	200
Figure 6.24: Plot of the mean tumors size measured using the RECIST criteria versus time.	201
Figure 6.25: Plot of the mean tumors size measured using the RECIST criteria versus lobe location.	202

Figure 6.26: Plot of the mean tumors size measured using the RECIST criteria versus time for each lobe.	203
Figure 6.27: Percentage histogram for the mean tumor size measured using the RECIST criteria.	204
Figure 6.28: Percentage histogram for the mean tumor size measured using the RECIST criteria for each lobe.	204
Figure 6.29: Percentage histogram for the mean tumor size measured using the RECIST criteria at each time point.	205
Figure 6.30: Disappearing nodule illustration. (a-b) represents the identified nodule at month 2, and (c-d) represents the same region post registration with no nodule. (a) and (c) represent screen shot from Siemens OncoCare nodule segmentation package, and (b) and (d) represents a magnified image of the appropriate transverse slice from the bottom left sub-image of each time point.	207
Figure 6.31: (a) 18F-FDG PET scan of a Urethane mouse at the 6-month time point, (b) 18F-FLT PET scan of the same mouse at the same time point, and (c) 18F-FDG PET scan of the same mouse at the 9-month time point. Window and level are constant across images.	208
Figure 6.32: Registered micro-CT lung dataset from the same mouse shown in Figure 6.31 at 6 and 9 months in (a) and (b), respectively. (c) Illustrates the 3D reconstruction of the lung volume at 6 (blue) and 9 (red) months. Clearly the lung volume has significantly increased.	208
Figure 6.33: Transverse thoracic image of the same Urethane mouse using the (a) micro-CT and (b) micro-MRI system, respectively (scans acquired one day after another). As seen tumors indicated and labeled 2, 3 and 4 are visible in both the micro-CT and micro-MRI image, while nodule 1 is only visible in the micro-CT image.	209
Figure 6.34: CBCM images from (a) normal A/J mouse and (b-d) Urethane mouse lung at the 6-month time point, (a) non-suspicious region from normal A/J mouse, (b) non-suspicious region from Urethane mouse (c) suspicious alveolar region from Urethane mouse, (d) large peripheral tumor from Urethane mouse.	210

- Figure 6.35: LSCM images from a normal A/J and a Urethane mouse lung at 6-months using the custom imaging chamber, (a) normal A/J mouse lung parenchyma, (b) ‘normal’ parenchyma from a Urethane mouse lung surrounding a micro adenoma and (c) tumor region from Urethane mouse lung. Image scale consistent across tiled examples..... 212
- Figure 6.36: Low magnification (4x objective) LSCM image of a tumor from a Urethane mouse at 6-months. Tumor located at the base of the left lung..... 213
- Figure 6.37: LSCM images from a Urethane mouse lung at 6-months using the custom imaging chamber, (a) normal alveolar tissue, (b) tumor tissue. Image scale consistent across examples..... 214
- Figure 6.38: Urethane mouse lung tumor at 6-months, imaged using the LSCM imaging chamber technique with PKH26-PCL macrophage labeling..... 214
- Figure 6.39: Heitzman fixed, foam embedded Urethane mouse lung micro-CT dataset. 24 images with 28 microns thickness and 500 micron spacing between images are shown from the apex to base of the lung, top to bottom, left to right respectively. 216
- Figure 6.40: Heitzman fixed, foam embedded Urethane mouse lung LIMA complete dataset. Each tile represents an en bloc image acquired prior to a 500 micron section from the apex to base of the lung, top to bottom, left to right respectively. 217
- Figure 6.41: Heitzman fixed, foam embedded Urethane mouse lung H&E Histology dataset. Each tile represents a 5 micron thick section from the respective 500 micron LIMA section from the apex to base of the lung, top to bottom, left to right respectively..... 218
- Figure 6.42: Registered (a) *in vivo* micro-CT, (b) fixed *ex vivo* micro-CT, (c) LIMA and (d) H&E Histology dataset from the six-month time point..... 219
- Figure 6.43: Micro-CT axial images at 2, 3 and 4 months post Urethane administration for the dataset shown in Figure 6.42. 220
- Figure 6.44: Urethane mouse lung histology at 6-months (a-d) normal parenchyma, (e-h) alveolar hyperplasia, (i-l) benign micro adenoma (<0.5mm), (m-p) benign

papillary adenoma (>0.5mm), (q-t) pre-invasive adenoma (>1mm), (u-x) malignant adenocarcinoma at 12 months (>5mm)..... 221

Figure 6.45: Tumor progression from three lesion identified in the left lung of the Urethane mouse lung shown in Figure 6.39, Figure 6.40 and Figure 6.41..... 222

Figure 6.46: Magnified cascading (4x, 10x and 20x) histology from three six-month lesions as tracked and graphed in Figure 6.45. Panel (a-c) represents tumor LL1_2_H, (d-f) represents tumor LL1_1_S, and (g-i) represents tumor LL1_4_P. 223

Figure 6.47: CBCM image over a tumor region with (a) no pressure applied to the probe and (b) with slight pressure applied to the probe..... 235

List of Tables

Table 1. Density profile slope comparison.....	120
Table 2. Right Main Bronchus Density profile slope comparison.....	121
Table 3: Tumor Descriptive Statistics.....	195
Table 4: Tumor incidence and lobe volume versus lobe location.	199
Table 5: RECIST statistics for lung tumors versus scan time.....	201
Table 6: RECIST statistics of tumor size versus anatomical lobes.	202
Table 7: RECIST statistics for each lobe at each time point.....	203

List of Symbols and Abbreviations

ν	Frequency
λ	Wavelength
18F-FDG	Fluodeoxyglucose F18
18F-FLT	Fluorothymidine F18
A/D	Analog-to-Digital
AOTF	Acousto-Optical Tunable Filter
BASC	Bronchio-Alveolar Stem Cell
c	Speed
CBCM	Catheter Based Confocal Microscopy
CCD	Charge Coupled Device
cGy	Centi-Gray
CT	Computed Tomography
DPSS	Double Pumped Solid State
dsDNA	Double Stranded DNA
E	Energy
EM	Electro Magnetic
eV	electron Volt
FFT	Fast Fourier Transform
FOV	Field of View
GFP	Green Fluorescent Protein
GRE	Gradient-Recalled Echo
GRIN	Gradient-Index
HU	Hounsfield Unit
IFFT	Inverse Fast Fourier Transform
IIBH	Intermittent Iso-pressure Breath hold
IM	Intra Muscular
IP	Intra Peritoneal
IV	Intra Venous
LE	Late Expiratory
LI	Late Inspiratory
LIMA	Large Image Microscope Array
LSCM	Laser Scanning Confocal Microscopy

MCL	Mean Chord Length
MCLa	Mean Chord Length of Airspace
MCLw	Mean Chord Length of Wall
MEMS	Micro Electro Mechanical System
micro-CT	micro-Computed Tomography
MRI	Magnetic Resonance Imaging
MTF.....	Modular Transfer Function
NSCLC	Non-Small-Cell Lung Cancer
PBS.....	Phosphate Buffer Saline
PID	Proportional Integrative Derivative
PMT.....	Photo Multiplier Tube
RECIST	Response Evaluation Criteria in Solid Tumors
rtTA.....	Reverse Tetracycline Transactivator
SCLC.....	Small-Cell Lung Cancer
SNR.....	Signal to Noise Ratio
ssDNA	Single Stranded DNA
TTL	Transistor-Transistor Logic
WHO	World Health Organization

